Journal of Solid State Chemistry 184 (2011) 3247–3252

Contents lists available at SciVerse ScienceDirect

Journal of Solid State Chemistry

journal homepage: www.elsevier.com/locate/jssc

Crystal structure of $Na_2MMgP_2O_8$ (M: Ba, Sr, Ca) orthophosphates and their luminescence properties activated by Eu^{2+}; analogous structural behaviors of glaserite-type phosphates and silicates

Yoshinori Yonesaki*, Chihiro Matsuda

Interdisciplinary Graduate School of Medicine and Engineering, University of Yamanashi, Miyamae 7-32, Kofu 400-8511, Japan

ARTICLE INFO

Article history:
Received 9 August 2011
Received in revised form
7 October 2011
Accepted 8 October 2011
Available online 15 October 2011

Keywords:
Phosphor
Structure analysis
Phosphate
Glaserite
Blue emission

ABSTRACT

Rietveld refinements of X-ray powder diffraction data and vibrational spectroscopy have confirmed the crystal structure of $Na_2MMgP_2O_8$ (M: Ba, Sr, Ca) prepared by a standard solid state reaction. They have glaserite-type layered structure. $Na_2MMgP_2O_8$ has a trigonal $P\bar{3}$ form for M=Ba, and monoclinic $P2_1/c$ forms for M=Sr and Ca. The observed structural transition is analogous to the corresponding layered orthosilicate $M_3MgSi_2O_8$.

Eu^{2+}-doped $Na_2MMgP_2O_8$ exhibits an intense blue to violet emission under ultraviolet excitation, based on $5d$–$4f$ electron transition of Eu^{2+} ions. The emission character is very sensitive to the structural transition induced by M^{2+} and the subsequent site symmetry changes.

1. Introduction

Phosphors are utilized for various purposes in our daily life, such as interior lamps, light sources for displays, paints for sign boards and so forth. Most of commercially available phosphors are obtained by doping transition metal or rare-earth metal ions into a host crystalline material. In particular, Eu^{2+} ion is a very important activator because of the intense emission and color controllability. Eu^{2+} emission originates in parity-allowed $5d \rightarrow 4f$ electron transition. Since energy band of the $5d$ orbitals is energetically affected by symmetry and strength of the crystal field, Eu^{2+} emission strongly depends on host material. For a few decades, Eu^{2+}-doped glaserite-type orthosilicates $M_3MgSi_2O_8$ (M: Ba, Sr, Ca) have been focused on as candidates for high performance phosphors, and there are many reports on their great potential for the intense blue emission [1–18]. Our group has also investigated their emission properties in terms of the crystal structure [7,13,16,18]. Fig. 1 shows a schematic illustration of the glaserite-type $BaCa_2MgSi_2O_8$ structure [7,17]. The layer is built up by corner-sharing of MgO_6 octahedra and SiO_4 tetrahedra, and Ba^{2+} and Ca^{2+} ions occupy interlayer sites. Larger alkaline-earth cations tend to occupy the interlayer A-site while smaller ones are prone to be at the layer-embedded B-site. It is noteworthy that in this type of silicates, interlayer A-site cations determine the crystal system. $M_3MgSi_2O_8$ crystallizes in trigonal system ($P\bar{3}$ or $P\bar{3}m1$) for larger A-site cations and in monoclinic system ($P2_1/c$) for smaller ones. Eu^{2+}-doped $M_3MgSi_2O_8$ shows an intense blue emission under UV excitation. The emission drastically changes in response to the crystal system; trigonal or monoclinic.

Recently, emission properties of Eu^{2+}-doped $Na_2CaMgP_2O_8$ have been reported by Lű et al. [19]. This phosphate exhibited blue emission under ultraviolet excitation. Interestingly, this compound has glaserite-type monoclinic layered structure (S.G., $P2_1/c$), in which interlayer A-site and layer-embedded B-site are occupied by Ca^{2+} and Na^{+}, respectively [20]. This report encourages us to find the presence of a highly ordered glaserite-type phosphates, in analogy with $M_3MgSi_2O_8$ orthosilicates. In the present study, the detail on the crystal structure of $Na_2MMgP_2O_8$ (M: Ba, Sr, Ca), in which interlayer A-site is occupied by M^{2+} ions, are described. Furthermore, the emission properties of the corresponding compounds doped with Eu^{2+} ions are discussed based on the solved structure.

2. Experimental

2.1. Synthesis

$Na_2MMgP_2O_8$ (M: Ba, Sr, Ca) crystalline powder samples were prepared from reagent grade Na_2CO_3, MCO_3 (M: Ba, Sr, Ca), magnesium carbonate hydroxide and $NH_4H_2PO_4$. A small amount

* Corresponding author. Fax: +81 55 254 3035.
E-mail address: yonesaki@yamanashi.ac.jp (Y. Yonesaki).

0022-4596/$ - see front matter © 2011 Elsevier Inc. All rights reserved.
doi:10.1016/j.jssc.2011.10.011

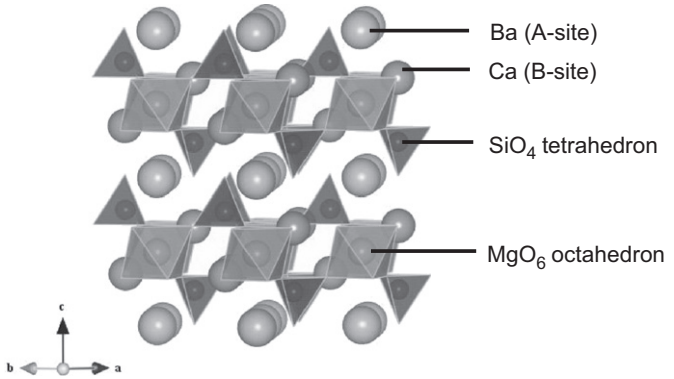

Fig. 1. Crystal structure of $BaCa_2MgSi_2O_8$, illustrated with MgO_6 octahedra and SiO_4 tetrahedra.

of NH_4Cl was used as a flux. Stoichiometric amounts of the reagents and the flux were ground and mixed by ball milling with zirconia beads in 2-propanol for 4 h. The mixed powder was heated at 1100 °C for 4 h in air with an intermittent re-grinding. The powder of $Na_2M_{0.98}Eu_{0.02}MgP_2O_8$ was prepared by heating stoichiometric mixture of the starting reagents and Eu_2O_3 at 1100 °C for 4 h in a flow of 2% H_2–98% N_2 gas with an intermittent re-grinding.

2.2. X-ray diffraction analysis

The prepared samples were investigated by X-ray powder diffraction (XRD) with a Rigaku RINT-2200HFV diffractometer using Cu$K\alpha$ radiation (λ=1.54058 Å). The structural refinement was carried out with the XRD data collected at intervals of 0.02° from 10° to 120° 2θ at room temperature. Lattice parameters and structure parameters were refined by Rietveld method using a program RIETAN-FP [21]. Figures of crystal structure in this paper were drawn with VESTA [22].

2.3. Raman spectroscopy

Room-temperature Raman spectra were measured for the prepared samples in backscattering geometry by a 3000 grooves/mm grating monochromator and a charge-coupled device detector system (RENISHAW, inVia Reflex system). Samples were excited with the 488-nm laser line of a 50 mW Spectra-Physics Cyan^{TM} Scientific CW laser. The laser beam was plain-polarized with a polarizer and focused on a sample with a 50× lens. A spectral resolution was 0.5 cm^{-1}. The laser power was attenuated to 5 mW before sample irradiation.

2.4. Photoluminescence

Emission spectra were measured for the prepared samples at room temperature using a JASCO corporation FP-6500 spectrofluorometer.

3. Results

3.1. Crystal structure of $Na_2MMgP_2O_8$

Fig. 2 shows the XRD patterns for the $Na_2MMgP_2O_8$ samples. The $Na_2CaMgP_2O_8$ pattern agrees well with the previous data [19]. Although a small amount of impurity phase can be seen in the sample of $Na_2BaMgP_2O_8$, the main reflections are indexed with a hexagonal unit cell with a=5.3043(9) Å and c=6.9915(8) Å for $Na_2BaMgP_2O_8$, and with a monoclinic unit cell with a=9.124(3) Å, b=5.279(15) Å, c=13.499(4) Å and β=90.013(5)° for $Na_2SrMgP_2O_8$. Using glaserite-type families as initial structure model, the crystal structure of $Na_2BaMgP_2O_8$ and $Na_2SrMgP_2O_8$ has been successfully refined (the final profile fits are attached as supplementary materials). The crystal data and atomic parameters are listed in Tables 1 and 2, respectively. Lattice constants for the trigonal $P\bar{3}$ cell can be converted to the corresponding monoclinic $P2_1/c$ cell with the relation that $a_m=\sqrt{3}a_t$, $b_m=b_t$ and $c_m=2c_t$ (subscript "m" means monoclinic and "t" trigonal). To check the reasonability of the refined structure, vibrational spectroscopy was attempted for them. Fig. 3 shows the Raman spectra of the $Na_2MMgP_2O_8$ samples. Intense Raman peaks appear at about 1000, 440, 1120 and 590 cm^{-1}. Generally, Raman peaks at such high wavenumbers (>400 cm^{-1}) are attributed to internal vibrations of certain atomic groups. In the present case, they are derived from the four normal modes of PO_4 tetrahedra; symmetric stretching vibration ν_1,

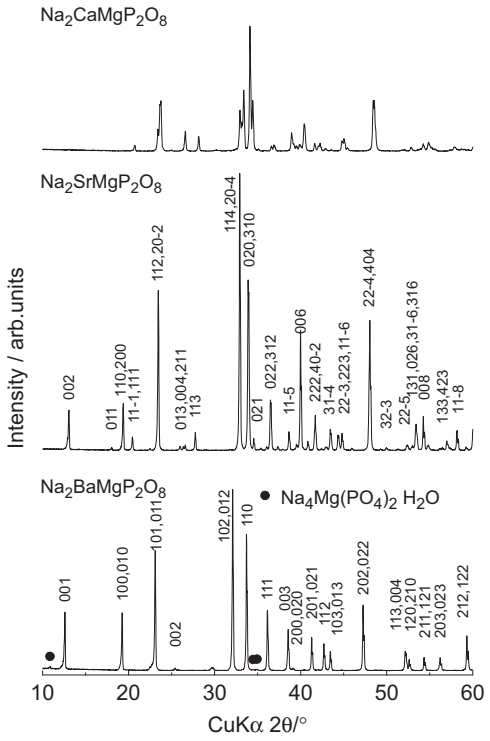

Fig. 2. X-ray powder diffraction patterns for the prepared samples. For the samples of M=Sr and Ba, diffraction peaks from the $Na_2MMgP_2O_8$ phase are indexed.

Table 1
Crystallographic data for $Na_2MMgP_2O_8$ (M: Ba, Sr).

M	Ba	Sr
Empirical formula	$Na_2BaMgP_2O_8$	$Na_2SrMgP_2O_8$
Formula weight	397.55	347.85
Crystal system, space group	Trigonal, $P\bar{3}$ (no. 147)	Monoclinic, $P2_1/c$ (no. 14)
Unit cell parameters	a=5.3043(9) Å	a=9.124(3)
	c=6.9915(8) Å	b=5.279(15)
		c=13.499(4)
		β=90.013(5)
Volume (Å^3)	170.36(4)	650.3(3)
Z	1	4
Calculated density (g cm^{-3})	3.88	3.55
R_p (%)	9.86	12.25
WR_p (%)	14.13	16.18
R_I (%)	3.87	6.44
R_F (%)	1.75	3.83

Table 2
Atomic coordinates and isotropic displacement parameters for $Na_2BaMgP_2O_8$ (a) and for $Na_2SrMgP_2O_8$ (b).

Atom	Site	x	y	z	B_{iso} (Å^2)
(a) $Na_2BaMgP_2O_8$					
Na	2*d*	1/3	2/3	0.8217(8)	0.8(11)
Ba	1*b*	0	0	1/2	0.61(4)
Mg	1*a*	0	0	0	1.1(13)
P	2*d*	1/3	2/3	0.2612(5)	0.27(9)
O1	2*d*	1/3	2/3	0.472(14)	0.3(11)
O2	6*g*	0.223(12)	−0.131(12)	0.1761(6)	$=B_{iso}$(O1)
(b) $Na_2SrMgP_2O_8$					
Na1	4*e*	0.087(2)	0.221(2)	0.4112(8)	0.2(13)
Na2	4*e*	0.410(2)	0.313(2)	0.0907(9)	$=B_{iso}$(Na1)
Sr	4*e*	0.7538(6)	0.2961(6)	0.2494(4)	1.13(6)
Mg	4*e*	0.753(2)	0.216(2)	0.004(10)	0.2(15)
P1	4*e*	0.085(17)	0.279(19)	0.1273(9)	0.57(9)
P2	4*e*	0.405(19)	0.260(2)	0.3649(8)	$=B_{iso}$(P1)
O1	4*e*	0.087(3)	0.797(4)	0.404(18)	0.4(12)
O2	4*e*	0.071(3)	0.222(3)	0.242(16)	$=B_{iso}$(O1)
O3	4*e*	0.158(3)	0.545(5)	0.110(12)	$=B_{iso}$(O1)
O4	4*e*	0.157(3)	0.066(4)	0.071(12)	$=B_{iso}$(O1)
O5	4*e*	0.366(3)	0.007(4)	0.414(13)	$=B_{iso}$(O1)
O6	4*e*	0.444(2)	0.206(4)	0.255(16)	$=B_{iso}$(O1)
O7	4*e*	0.591(3)	0.289(4)	0.404(18)	$=B_{iso}$(O1)
O8	4*e*	0.657(4)	−0.018(4)	0.097(13)	$=B_{iso}$(O1)

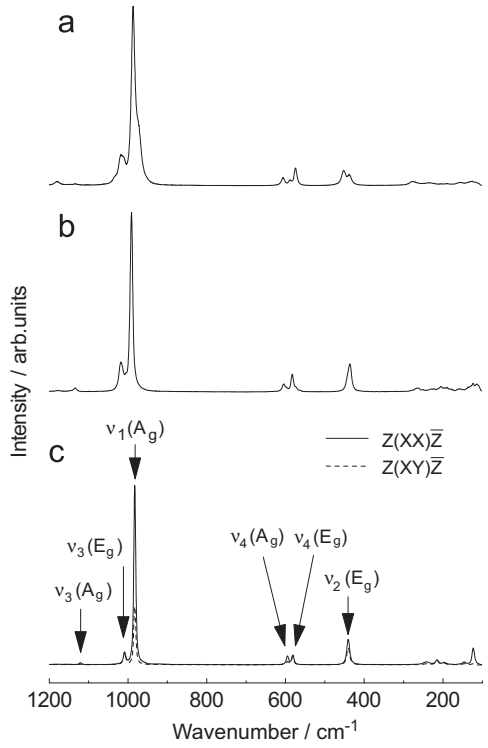

Fig. 3. Raman spectra for the prepared $Na_2MMgP_2O_8$. $Z(XX)\bar{Z}$ and $Z(XY)\bar{Z}$ correspond to $I_{\parallel}$ and $I_{\perp}$, respectively. (a) $Na_2CaMgP_2O_8$, (b) $Na_2SrMgP_2O_8$ and (c) $Na_2BaMgP_2O_8$.

symmetric bending vibration ν_2, asymmetric stretching vibration ν_3 and asymmetric bending vibration ν_4. For $Na_2BaMgP_2O_8$, the number of the PO_4-derived internal modes (peak numbers) agrees with the results of factor group analysis for the refined structure (Fig. 4(a); six PO_4-derived Raman-active modes in high wavenumber region). This agreement supports the refined $Na_2BaMgP_2O_8$ structure. For $Na_2SrMgP_2O_8$, the peak number in the Raman spectrum is less than that expected from the factor group analysis (Fig. 4(b); 36 PO_4-derived Raman-active modes in high wavenumber region). It is due to that non-degenerated Raman peaks do not split enough since $Na_2SrMgP_2O_8$ has an orthorhombic-like monoclinic cell ($\beta \fallingdotseq 90^\circ$). From the spectral comparison, it has been revealed that $Na_2SrMgP_2O_8$ has intermediate structure of trigonal $Na_2BaMgP_2O_8$ and monoclinic $Na_2CaMgP_2O_8$.

For $Na_2BaMgP_2O_8$, the calculated vibrational modes (Fig. 4(a)) are assigned to the observed Raman peaks, based on depolarization ratio ρ_p given by

$$\rho_p = \frac{I_{\perp}}{I_{\parallel}}. \quad (1)$$

Here $I_{\perp}$ and $I_{\parallel}$ are the Raman peak intensities under perpendicular and parallel configurations of polarizer and analyzer, respectively. If crystalline particles are randomly oriented, ρ_p is equal to 3/4 for nontotally symmetric vibrations and smaller than 3/4 for totally symmetric vibrations [23]. From the comparison of ρ_p, the peaks at 983.1, 1123.1, 595.1 cm^{-1} are A_g modes derived from ν_1, ν_3 and ν_4-vibration, respectively. The peaks at 440.9, 1008.4 and 581.5 cm^{-1} are E_g modes derived from ν_2, ν_3 and ν_4, respectively.

3.2. Emission properties

Eu-doped $Na_2MMgP_2O_8$ exhibited intense blue to violet emissions under ultraviolet irradiation. Fig. 5 shows the emission spectra for the Eu-doped samples. All the samples show broad emission bands from 350 to 500 nm those arise from 5*d*–4*f* electron transition in divalent europium ions. It is worth noting that monoclinic $Na_2MMgP_2O_8$: Eu^{2+} (M=Sr, Ca) show asymmetric or split emission peaks. It is due to the fact that Eu^{2+} ions occupy at least two crystallographically different sites. The emission spectra for the monoclinic compounds can be successfully reproduced by two Gaussian peaks (Fig. 5 with broken lines). The fitting results are shown in Table 3. One centered at about 395 nm and the second at a longer wavelength. The 395-nm peak exhibits no significant shift while full width at half maximum (FWHM) changes. The area fraction to the total peak increases with M^{2+} size increasing. On the other hand, the longer-wavelength emission shows red shift with an increase in M^{2+} size although FWHM are rarely different. As for the trigonal $Na_2BaMgP_2O_8$, the emission spectrum could not be fitted with one Gaussian peak profile. It may reflect multi-site occupation of Eu^{2+} ions. Fig. 6 shows the excitation spectra for both tails of the overall emission band. Each spectrum reflects the split 5*d*-bands of Eu^{2+} at each crystallographic site. The excitation spectra for both emission sides have similar shape with each other. Energy transfer processes possibly occurred between crystallographically different Eu^{2+} ions. Indeed, spectral overlap is observed between shorter-wavelength emission band (Fig. 5) and excitation band for the longer-wavelength emission (Fig. 6). The shorter-wavelength emission of the trigonal $Na_2BaMgP_2O_8$ has narrower but efficient excitation bands (280–310 nm) compared with monoclinic $Na_2CaMgP_2O_8$ or $Na_2SrMgP_2O_8$. This point is discussed later in terms of the crystal structure.

4. Discussion

4.1. Crystal structure

Fig. 7 shows the refined crystal structure of $Na_2MMgP_2O_8$. $Na_2MMgP_2O_8$ has glaserite-type layered structure. Between the layers, interlayer site (A-site) and layer-embedded sites (B-site) exist. A divalent M^{2+} ion preferentially occupies A-site and Na^+ ion B-site. When A-site is occupied by a relatively small M^{2+} ion (Ca^{2+}), SiO_4 tetrahedra and MgO_6 octahedra tilt to form corrugated layers, which induces monoclinic distortion. Then,

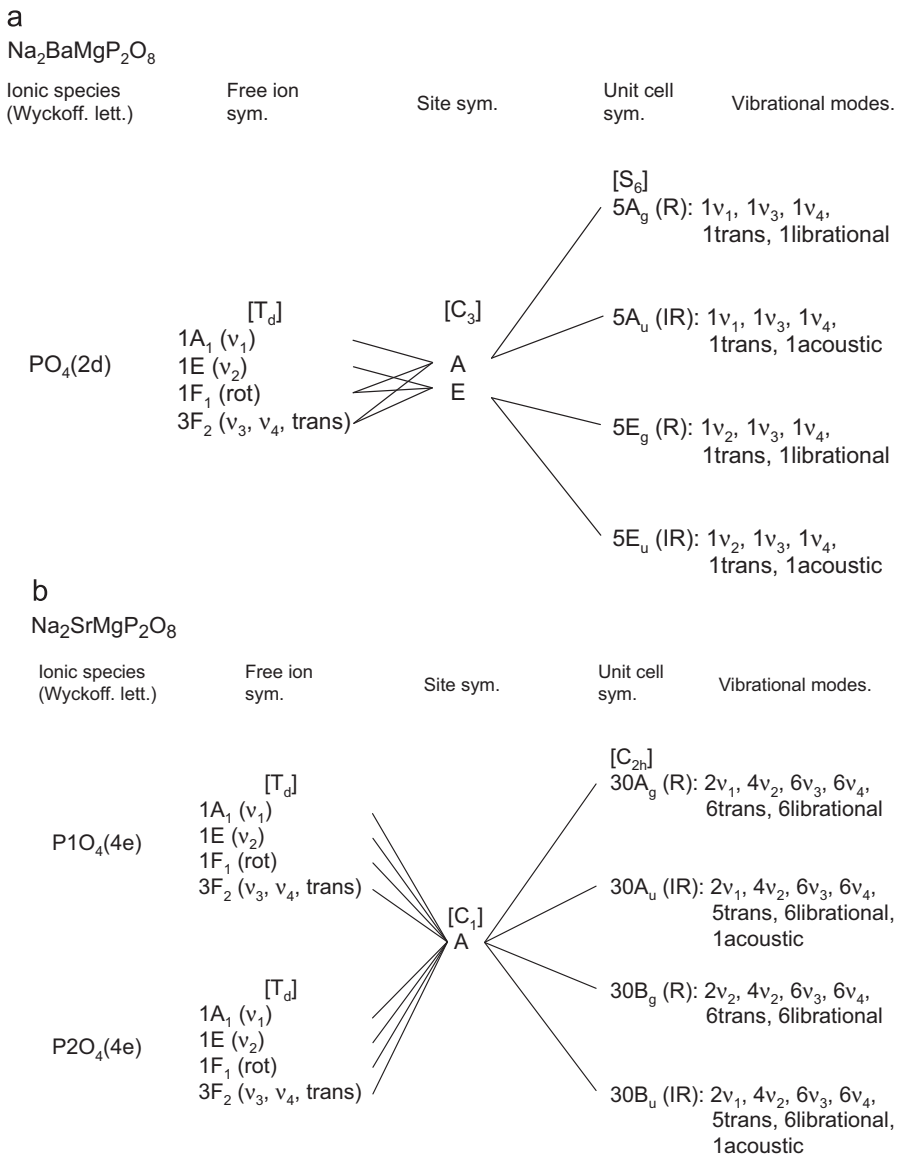

Fig. 4. Correlation tables for the refined $Na_2MMgP_2O_8$ structure (M=Ba (a) and Sr (b)). (R: Raman active, IR: IR active).

$Na_2MMgP_2O_8$ crystallizes in space group $P2_1/c$. As M^{2+} ion becomes large (Sr^{2+}), the lattice constant β approaches to 90° and layer-framework becomes flat. When a large Ba^{2+} ion occupies A-site, P–O1 bond becomes perpendicular to the flat layers, leading to the highly ordered $P\bar{3}$ structure. This type of structural transition is analogous to those for $M_3MgSi_2O_8$ orthosilicates [13]. According to the case of $M_3MgSi_2O_8$ orthosilicates, A-site is spatially limited by six oxide ions in lateral direction and by the distance between MgO_6 octahedra on upper and lower layers in vertical direction. The distances between an A-site cation and the six lateral oxide ions are so long that the flat layers can be maintained only when a large Ba^{2+} ion occupies A-site. If Sr^{2+} or Ca^{2+} ion occupies A-site, a large estrangement occurs especially in lateral direction. Then, the deformation from $P\bar{3}$ to $P2_1/c$ occurs to eliminate the estrangement. Also in the present orthophosphate, similar structural distortion may occur, depending on interlayer M^{2+} size. Fig. 8 shows the coordination environment around the Ba^{2+} ion in $Na_2BaMgP_2O_8$. The lateral Ba–O distance (Ba–O1) is equal to the value estimated from Shannon's ionic radii [24]. However, this room is too large for Sr^{2+} or Ca^{2+}.

4.2. Photoluminescence from Eu-doped $Na_2MMgP_2O_8$

As shown in Fig. 5, Eu-doped $Na_2MMgP_2O_8$ showed Eu^{2+}-derived emission under UV excitation. Their emission spectra indicated that Eu^{2+} ions occupied more than one site. Since the emission spectra could be reproduced by two Gaussian peaks, it is considered that Eu^{2+} ions replaced two crystallographically different sites. Lű et al. assigned the observed two-peak emission to two distinct Ca-sites [19]. However, $Na_2CaMgP_2O_8$ has only one independent Ca-site in the unit cell [20], which is not consistent with their assignment. We speculate that the two emission peaks corresponded to the Eu^{2+} ions at both A- and B-sites in the monoclinic $Na_2MMgP_2O_8$. Probably, the 395-nm emission is attributed to the Eu^{2+} ions at A-site and the longer-wavelength emission to Eu^{2+} ions at B-site from the following reason: according to Shannon, the ionic radii are arranged as $Ca^{2+} < Na^{+} < Eu^{2+} \fallingdotseq Sr^{2+} < Ba^{2+}$ [24]. Ca^{2+} ion has an ionic radius smaller than Eu^{2+} while Sr^{2+} is roughly the size of Eu^{2+}. Therefore, between $Na_2CaMgP_2O_8$ and $Na_2SrMgP_2O_8$, a remarkable difference is expected for the amount of Eu^{2+} ions

occupying A-site. From Fig. 5, it can be confirmed that the area fraction of the 395-nm peak was much lower for $Na_2CaMgP_2O_8$ than for $Na_2SrMgP_2O_8$, which shows the 395-nm peak corresponded to the Eu^{2+} at A-site. The red shift observed for the longer-wavelength emission was considered to be caused by ligand field change associated with the transition of lattice constant β.

Next, we focus on the difference between the trigonal compound (M=Ba) and the monoclinic compounds (M=Sr, Ca). As described in the results section, it is considered that $Na_2BaMgP_2O_8$ contained Eu^{2+} ions both at A- and B-site. The emission spectrum assures that their ligand fields were comparable level (emission wavelengths matched), which lead to intense emission. Fig. 6 shows that $Na_2BaMgP_2O_8$ had narrow but efficient excitation bands for the 395-nm emission, which can be interpreted in terms of site symmetry. In response to $Na_2MMgP_2O_8$ phase transition from $P2_1/c$ to $P\bar{3}$, A-site symmetry changes from C_1 to S_6. Under C_1 symmetry, the five 5d-orbitals of Eu^{2+} energetically split into five sets without any degeneracy (5a), which generates broad excitation bands. However, under S_6 symmetry, they split into three sets; two doubly degenerated sets e_g and one non-degenerated set a_g. Then, 5d-bands accumulate at three regions, but excitation efficiency increases because of the high density of states at the doubly degenerated e_g levels.

The prepared $Na_2MMgP_2O_8$:Eu^{2+} exhibited emission at shorter wavelengths than the glaserite-type orthosilicates $M_3MgSi_2O_8$:Eu^{2+} [13], despite their structural similarity. It may be caused by the difference in electron density of oxide ions. Because of the high electronegativity [25], phosphorus withdrew electrons from the surrounding oxide ions, which weakens electrostatic influences on Eu^{2+} ions in $Na_2MMgP_2O_8$.

5. Conclusions

Emission properties of Eu^{2+}-doped $Na_2MMgP_2O_8$ (M: Ba, Sr, Ca) have been discussed in terms of the crystal structure. $Na_2MMgP_2O_8$ has glaserite-type layered structure in which M^{2+} ion sites at interlayer A-site and Na^+ ion at layer-embedded B-site. $Na_2MMgP_2O_8$ crystallizes in $P\bar{3}$ trigonal structure for M=Ba and in $P2_1/c$ for M=Sr and Ca.

Under UV excitation, Eu^{2+}-doped $Na_2MMgP_2O_8$ exhibits blue to violet emission. A detailed analysis of the emission spectra reveals that the observed emission consists of the superposition of the

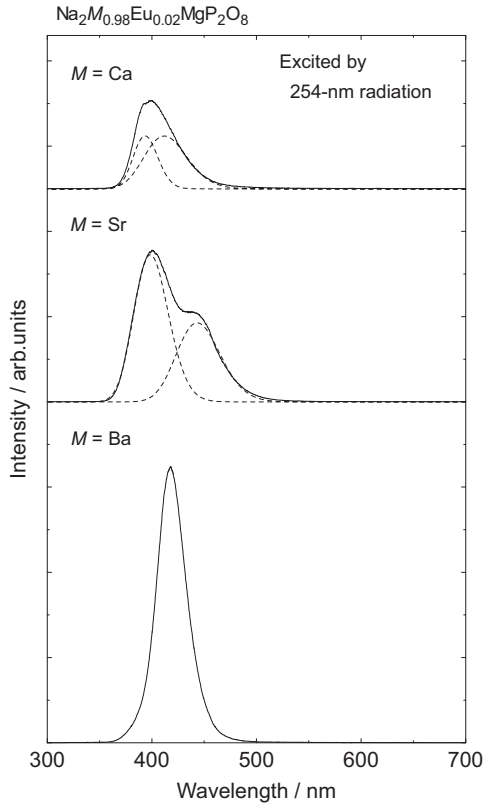

Fig. 5. Emission spectra for the Eu-doped $Na_2MMgP_2O_8$ samples. Broken lines for M=Sr and Ca show the separated emission peaks with Gaussian shape.

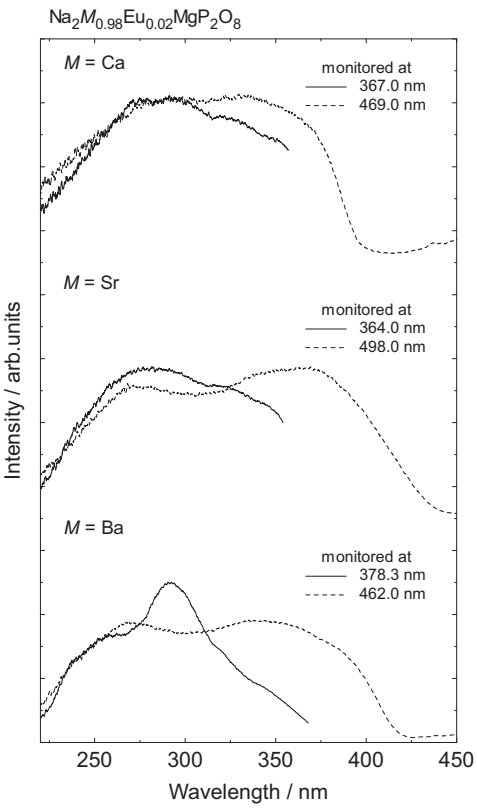

Fig. 6. Excitation spectra for both tails of the whole emission peak for the Eu-doped $Na_2MMgP_2O_8$ samples.

Table 3
Separated emission peak data of Eu-doped $Na_2MMgP_2O_8$ (M: Sr, Ca).

	$Na_2Ca_{0.98}Eu_{0.02}MgP_2O_8$		$Na_2Sr_{0.98}Eu_{0.02}MgP_2O_8$	
	Short wavelength	Long wavelength	Short wavelength	Long wavelength
Peak wavelength (nm)	393.5	411.9	398.4	443.3
FWHM of the emission peak (cm^{-1})	7.54×10^2	1.20×10^3	1.03×10^3	1.06×10^3

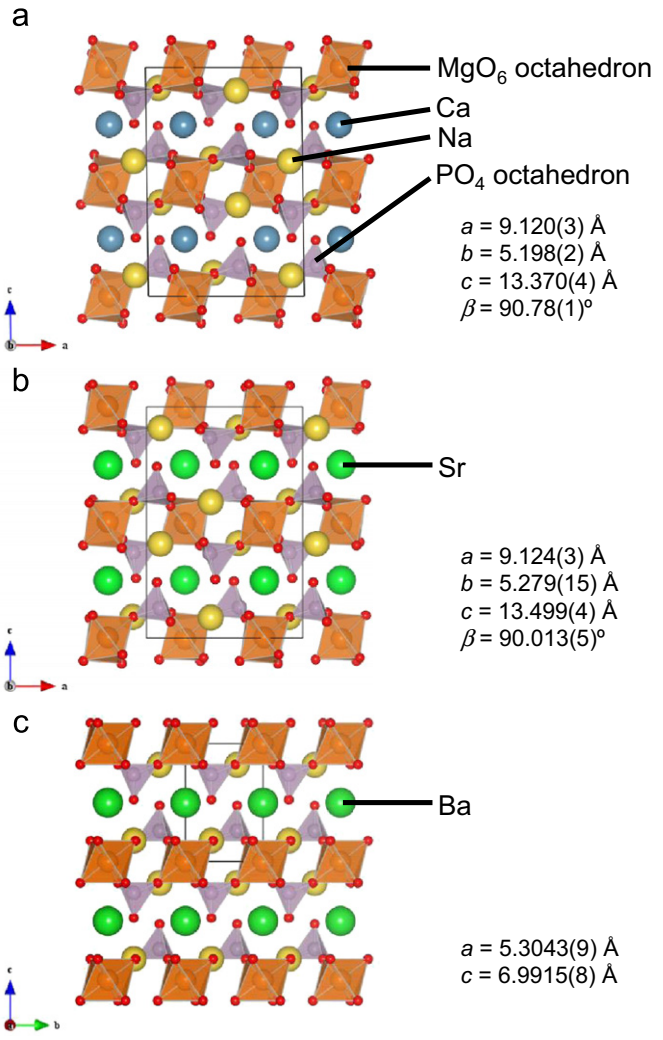

Fig. 7. The refined crystal structure of $Na_2MMgP_2O_8$. The solid-line frame indicates the unit cell of each structure. The crystal structure of $Na_2CaMgP_2O_8$ is quoted from Ref. [20]. (a) *M*=Ca, (b) *M*=Sr and (c) *M*=Ba.

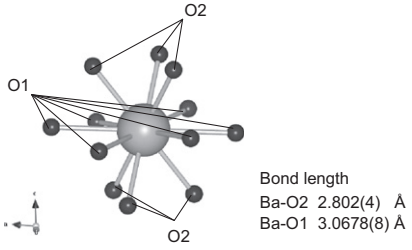

Fig. 8. Coordination environment around Ba^{2+} in $Na_2BaMgP_2O_8$.

emission character for both Eu^{2+} ions at A and B-site. Since the Eu^{2+} ions at B-site mainly contribute to a visible emission, it is important to design B-site environment for phosphor development.

Acknowledgments

The author Y. Yonesaki is indebted to the financial support for the present research by Nippon Sheet Glass Foundation for Materials Science and Engineering.

Appendix A. Supplementary materials

Supplementary materials associated with this article can be found in the online version at doi:10.1016/j.jssc.2011.10.011.

References

[1] G. Blasse, W.L. Wanmaker, J.W. Vrugt, A. Bril, Philips Res. Rep. 23 (1968) 189–200.
[2] T.L. Barry, J. Electrochem. Soc. 115 (1968) 733–738.
[3] J.S. Kim, J.Y. Kang, P.E. Jeon, J.C. Choi, H.L. Park, T.W. Kim, Jpn. J. Appl. Phys. 43 (2004) 989–992.
[4] J.S. Kim, K.T. Lim, Y.S. Jeong, P.E. Jeon, J.C. Choi, H.L. Park, Solid State Commun. 135 (2005) 21–24.
[5] H.K. Jung, K.S. Seo, Opt. Mater. 28 (2006) 602–605.
[6] J.S. Kim, A.K. Kwon, Y.H. Park, J.C. Choi, H.L. Park, G.C. Kim, J. Lumin. 122–123 (2007) 583–586.
[7] Y. Yonesaki, T. Takei, N. Kumada, N. Kinomura, J. Lumin. 128 (2008) 1507–1514.
[8] Y. Umetsu, S. Okamoto, H. Yamamoto, J. Electrochem. Soc. 155 (2008) J193–J197.
[9] S. Okamoto, Y. Nanba, T. Honma, J. Yamamoto, Electrochem. Solid-State Lett. 11 (2008) J47–J49.
[10] L. Ma, D.J. Wang, Z.Y. Mao, Q.F. Lu, Z.H. Yuan, Appl. Phys. Lett. 93 (2008) 144101.
[11] L. Ma, D.J. Wang, H.M. Zhang, T.C. Gu, Z.H. Yuan, Electrochem. Solid-State Lett. 11 (2008) E1–E4.
[12] D.J. Wang, L.Y. Liu, Electrochem. Solid-State Lett. 12 (2009) H179–H181.
[13] Y. Yonesaki, T. Takei, N. Kumada, N. Kinomura, J. Solid State Chem. 182 (2009) 547–554.
[14] W.B. Im, Y.I. Kim, H.S. Yoo, D.Y. Jeon, Inorg. Chem. 48 (2009) 557–564.
[15] C. Fu, Y. Hu, Y. Wang, H. Wu, X. Wang, J. Alloys Compd. 502 (2010) 423–428.
[16] Y. Yonesaki, T. Takei, N. Kumada, N. Kinomura, J. Solid State Chem. 183 (2010) 1303–1308.
[17] C.H. Park, T.H. Kim, Y. Yonesaki, N. Kumada, J. Solid State Chem. 184 (2011) 1566–1570.
[18] Y. Yonesaki, Q. Dong, N.S.B. Mohamad, A. Miura, T. Takei, J. Yamanaka, N. Kumada, N. Kinomura, J. Alloys Compd. 509 (2011) 8738–8741.
[19] J. Lű, Y. Huang, L. Shi, H.J. Seo, Appl. Phys. A 99 (2010) 859–863.
[20] J. Alkemper, H. Fuess, Z. Kristallogr. 213 (1998) 282–287.
[21] F. Izumi, K. Momma, Solid State Phenom. 130 (2007) 15–20.
[22] K. Momma, F. Izumi, J. Appl. Crystallogr. 41 (2008) 653–658.
[23] K. Nakamoto, Infrared and Raman Spectra of Inorganic and Coordination Compounds Part A: Theory and Applications in Inorganic Chemistry, fifth edn., Wiley-Interscience Publication, New York, 1997.
[24] R.D. Shannon, Acta Crystallogr. A 32 (1976) 751–767.
[25] J.E. Huheey, E.A. Keiter, R.L. Keiter, Inorganic Chemistry Principles of Structure and Reactivity, fourth edn., HarperCollins College Publishers, New York, 1997.